ACADÉMIE
DES SCIENCES
INSTITUT DE FRANCE

Comptes Rendus
Chimie

Asmae El Maangar, Johannes Gramüeller, Verena Huber, Pierre Degot, Didier Touraud, Ruth Gschwind, Werner Kunz and Thomas Zemb

Solubilisation–microstructure relationship of trivalent salts in hydrotropic ternary systems

Volume 27, Special Issue S4 (2024), p. 185-202

Online since: 2 June 2025

Part of Special Issue: GDR Prométhée – French Research Network on *Hydrometallurgical Processes for Primary and Secondary Resources*

Guest editors: Laurent Cassayre (CNRS-Université de Toulouse, Laboratoire de Génie Chimique, France) and Hervé Muhr (CNRS-Université de Lorraine, Laboratoire Réactions et Génie des Procédés, France)

https://doi.org/10.5802/crchim.310

The Comptes Rendus. Chimie *are a member of the Mersenne Center for open scientific publishing*
www.centre-mersenne.org — e-ISSN : 1878-1543

ACADÉMIE DES SCIENCES
INSTITUT DE FRANCE

Comptes Rendus. Chimie
2024, Vol. 27, Special issue S4, p. 185-202
https://doi.org/10.5802/crchim.310

Research article

GDR Prométhée – French Research Network on *Hydrometallurgical Processes for Primary and Secondary Resources*

Solubilisation–microstructure relationship of trivalent salts in hydrotropic ternary systems

Asmae El Maangar [a], Johannes Gramüeller [b], Verena Huber [c], Pierre Degot [c], Didier Touraud [c], Ruth Gschwind [b], Werner Kunz [c] and Thomas Zemb [*, a]

[a] ICSM, Univ. Montpellier, CEA, CNRS, ENSCM, Marcoule, France

[b] Institute of Organic Chemistry, Faculty of Chemistry and Pharmacy, University of Regensburg, D-93040 Regensburg, Germany

[c] Institute of Physical and Theoretical Chemistry, Faculty of Chemistry and Pharmacy, University of Regensburg, D-93040 Regensburg, Germany

E-mail: thomas.zemb@icsm.fr (T. Zemb)

Abstract. We show here that there are four different regimes of pronounced mesoscopic structuring in the monophasic region of the water/sodium salicylate/ethyl acetate ternary phase diagram. Surprisingly, the solubility of various lanthanides is highest in these regimes containing pre-nucleation clusters and not in the complexation regime. All four local maxima of solubility are characterised by their scattering and explained in terms of the driving forces behind the structuring and as a function of the added ions. The position of the critical point was determined by regions where critical opalescence is maximal. After centrifugation, the points located at the boundary of the diphasic zone separate into two immiscible fluids of equal volumes.

While the highest solubility of metal ions is found in the region of critical fluctuations, a still high solubility combined with a significant selectivity was found in the region of the pre-nucleation clusters. This new and previously unknown feature can also be explained and may pave the way for a new, green procedure of selective rare-earth metal recovery.

Keywords. Separation chemistry, Critical fluctuations, Sodium salicylate, Lanthanides, Pre-Ouzo effect, Hydrotropes.

Funding. CNRS through the International Research Project "NISI" program, Fonds der Chemischen Industrie.

Manuscript received 23 October 2023, revised 23 April 2024, accepted 8 April 2024.

1. Introduction

Ternary systems comprising a short-chain amphiphilic molecule called "hydrotrope" and two immiscible fluids are considered as powerful solubilisation media avoiding the use of surfactants [1–3]. Hydrotropes are small, usually water-soluble, organic molecules [4]. They comprise hydrophilic and hydrophobic moieties, with the hydrophobic moiety being too small to induce micelle formation [5]. Typical examples include neutral compounds such as short-chain alcohols like ethanol, but also charged molecules, usually anionic compounds composed of an aromatic ring with an additional sulfate, sulfonate, or carboxylate group. Typical examples of hydrotropes are sodium salicylate

* Corresponding author

(NaSal), which is widely used in the pharmaceutical and body care industry, sodium xylene sulfonate (SXS), sodium cumene sulfonate (SCS) or sodium toluene sulfonate (NaTS). The existence of well-defined mesoscale inhomogeneities in macroscopically transparent solutions was shown to be often responsible for such unexpected solubilisation capacity. Such mesoscale inhomogeneity phenomena of oil-rich and water-rich domains are comparable to the microdomains observed in the classical water/oil/surfactant ternary systems (direct, bicontinuous, and reverse microemulsions) [1,3,6,7], and therefore we call the corresponding systems surfactant-free microemulsions (SFME).

The concept of hydrotropy, defined by Neuberg in 1916 [8,9], outlines the capability of short-chain amphiphilic molecules to solubilise hydrophobic compounds in a hydrophilic solvent. In SFME showing the compartmentation of hydrophilic and hydrophobic domains, the hydrotrope accumulates mostly at the interface between water-rich and oil-rich domains. The interface between the oil-rich and water-rich domains is usually considered as a kind of highly flexible film in dynamic exchange with the surrounding medium [3,10].

In contrast to surfactants, the amphiphilic character of hydrotropes is usually considered to be insufficiently pronounced to promote micellisation or self-aggregation of the hydrotrope itself in water [11]. However, they are able to form loose or ill-defined aggregates at higher concentrations (~1 M) than those that would be necessary for surfactants (10^{-2}–10^{-3} M). Sometimes the loose aggregation only happens when a hydrophobic solute is present. The solute is solubilised in binary or ternary solvents as isolated molecules, and it is not clear until now how aggregation enhances solubilisation [12]. Shimizu et al. described theoretically this hydrotropic solubilisation using an approach derived from pure statistical thermodynamics. They considered hydrotropic solubilisation to be the result of a subtle balance between hydrotrope–hydrotrope interaction and solute–hydrotrope interaction. In other studies, the authors argued that strong hydrotrope–hydrotrope interactions, resulting in a pre-structuring of the hydrotrope in H_2O, diminish the solubilisation efficiency of solutes [13,14]. However, the opposite was also found [7]. This solubilisation efficiency could also come from an entropic effect in the bulk of the solvent by preferential adsorption as recently shown by Spadian et al. [15]. As we will see in the following, things are even more complex.

Various examples of solubilisation with anionic hydrotropes are described in the literature: Theneskumar et al. have solubilised a highly hydrophobic compound, lauric acid, in water using different hydrotropes such as SCS, SXS and NaTS [16]. A high amount of hydrotrope (over 0.5 mol/L) was necessary to enhance the solubility of lauric acid by a factor of 6 at room temperature. The same hydrotropes also enhance the solubility of the water-insoluble hydroxyacetophenones [17]. NaSal was used to increase the solubility of salicylic acid in water [18] and is widely used in the pharmaceutical industry as hydrotrope [19–21].

From the phase diagram consisting of water, NaSal, and ethyl acetate (EA), as studied by El Maangar et al., it can be deduced that the hydrotrope is not soluble in the organic phase [22]. However, a monophasic domain was found, which is enclosed by a liquid/liquid and a solid/liquid two-phasic system (see Figure 1). The monophasic area was examined using density excess, X-ray, and neutron scattering techniques, and they evidenced three major facts. First, in an ethyl acetate saturated aqueous solution, the hydrotrope NaSal can indeed form aggregates which are reminiscent of micelles. Second, the critical point was determined to be close to the EA-rich corner of the phase diagram, surrounded by asymmetrical tie lines, and around the critical point neither a pre-Ouzo structuring nor a spontaneous Ouzo effect could be evidenced. This suggests that there is only a "normal" critical point in this phase diagram. Finally, in a domain near the liquid/solid phase boundary, X-ray, light, and neutron scattering combined with a density excess determination proved the presence of dynamic aggregates reminiscent of pre-nucleation clusters (PNC) [23]. These aggregates are stabilised without any surfactants but by selective solvation of ethyl acetate. These findings are intriguing and triggered the detailed examination of the nanostructuring occurring in the monophasic region as well as the evolution of the solubilisation capacity of charged trivalent electrolytes—lanthanide salts—by this ternary system in the single-phase region.

Our goal is to establish a structure–function relationship and to determine to what extent the microstructure influences the solubilisation of solutes

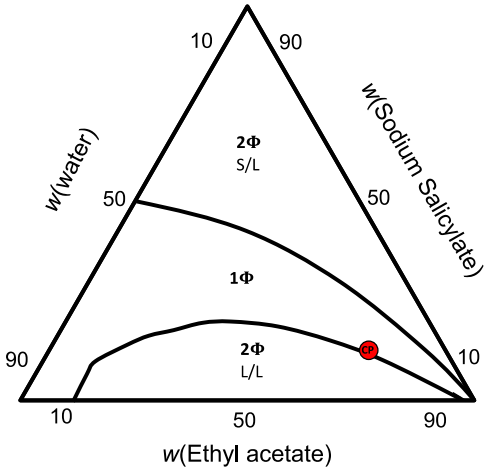

Figure 1. Ternary phase diagram of water, sodium salicylate, and ethyl acetate, showing the single phase-region present is separated by a binodal line from the 2-pahse region and a S/L region with an excess precipitate that is rich in sodium salicylate. The red dot indicates the critical point. The figure is adapted from [22].

and how this will be different for electrolytes and non-electrolytes.

2. Experimental section

2.1. *Materials*

Ethyl acetate (EA) (purity > 99.9%) was purchased from Merck. Sodium salicylate (NaSal) (purity > 99.5%) was purchased from Sigma Aldrich. All samples were prepared with deionised water using a Millipore Milli-Q purification system (Merck Millipore. Billerica. MA). All other chemicals were purchased from Sigma Aldrich: lanthanum (III) nitrate hexahydrate $La(NO_3)_3{\cdot}6H_2O$ (purity > 99.99%), neodymium (III) nitrate hexahydrate $Nd(NO_3)_3{\cdot}6H_2O$ (purity > 99.9%), europium (III) nitrate hexahydrate $Eu(NO_3)_3{\cdot}6H_2O$ (purity > 99.9%), dysprosium (III) nitrate hexahydrate $Dy(NO_3)_3{\cdot}6H_2O$ purity > 99.9%), and ytterbium (III) nitrate hexahydrate $Yb(NO_3)_3{\cdot}6H_2O$ (purity 99.9%). All chemicals were used without further purification.

2.2. *Phase diagrams*

All phase diagrams were determined with the cloud point method [24], by initially mixing sodium salicylate with one of the other two solvents, then adding the third one dropwise to the solutions, until a visible change in the phase behaviour occurred. The initial phase diagrams were determined in mass fractions w_i. To obtain the phase diagrams in molar fractions x_i, the molar masses of the pure solvents were used. All phase diagrams were determined at 25 °C, and the phase transitions were determined with the naked eye and through two cross-polarised filters to check the presence of liquid crystals.

We define compositions in the monophasic region based on a mass fraction relative to binary fluids: α is the mass fraction of EA in the water/EA binary mixture, not taking into account the amount of hydrotrope present in the sample for the determination of α. All additions were measured by weight with a laboratory scale. Solutions were prepared at room temperature.

2.3. *Density measurement and tie-line determination in the miscibility gap*

Solution densities were determined using a vibrating tube density meter (DMA 5000 M. Anton Paar. Austria) at (25 ± 0.005) °C with a nominal precision of $\pm 5 \times 10^{-6}$ g/mL. Calibration was performed using air and pure water at 25 °C. Calibration was checked using pure water and between each measurement against air (allowed deviation: $\pm 5 \times 10^{-5}$ g/ml).

The determination of the density allows determining the two extremities of the tie-lines in the biphasic liquid/liquid region very precisely, i.e., the phase boundary actually corresponds to the binodal (compositions of phases in contact at equilibrium). To this purpose, a mapping of more than a hundred samples was used after interpolation of the measured densities as explained in the work of El Maangar et al. [22], and thus the compositions of the two phases at equilibrium are obtained.

2.4. *Conductivity measurements*

Conductivity measurements were carried out in a thermostatic measurement cell (25.0 °C) under permanent stirring and if necessary, manual mixing using a low-frequency WTW inoLab Cond 730 conductivity meter connected with a WTW TetraCon 325 electrode (Weilheim, Germany). 20 g of initial sample were placed in the measurement cell and

successively diluted either with pure water or ethyl acetate. The electrode was calibrated with potassium chloride, and a cell constant of $R = 0.472$ cm^{-1} was determined.

2.5. *Diffusion-ordered NMR(DOSY) experiments*

Diffusion-ordered NMR spectroscopy experiments were performed on a Bruker Avance III HD 600 MHz spectrometer, equipped with a 5 mm CPPBBO BB-^{1}H/^{19}F probe. All measurements were performed at 298 K, and the temperature was controlled by a BVT 3000 and a BVTE 3900 temperature unit. NMR data were processed, evaluated, and plotted with the TopSpin 3.2 software.

Deuterated solvents were not employed, and no field-frequency lock was established. Due to the rather short measurement times, no drift of the chemical shifts was observed due to a missing field-frequency lock. To establish magnetic field homogeneity, shimming was performed on the ^{1}H NMR signals (either on the singlet of H_2O or ethyl acetate). ^{1}H NMR signals were not referenced.

Measurements were performed in the monophasic region (depicted in Figure 3). To this purpose 5 g samples were prepared and centrifuged at 4300 g for 10 min. Then the solutions were transferred to standard NMR tubes.

The DOSY measurements were performed with the convection-suppressing DSTE (double stimulated echo) pulse sequence developed by Jerschow and Müller in a pseudo 2D mode [25]. The diffusion time delay was set to 45 ms. Smoothed square (SMSQ10.100) gradient shapes and a linear gradient ramp with 20 increments between 5% and 95% of the maximum gradient strength (5.35 G/mm) were used. For the homospoil gradient strengths, values of 100, −13.17, 20, and −17.13% were used. For each compound in the sample, gradient pulse lengths were first optimised to obtain a sigmoidal signal decay for increasing gradient strength, with gradient pulse lengths ranging from 0.75 to 3.3 ms. NMR spectra were processed with Bruker TopSpin 3.2 (T1/T2 relaxation package), and diffusion coefficients were derived according to Jerschow and Müller [25].

2.6. *X-ray fluorescence (XRF) measurements*

For ternary systems containing organic compounds, X-ray fluorescence (XRF) is a precise and suitable method to quantify the elements present in the solution. The commercial XRF spectrometer used to analyse the samples after solubilising lanthanides is a SPECTRO XEPOS (AMETEK) model. It is commercially equipped with an energy dispersive X-ray analyser (ED-XRF) that uses the energy loss of the X photon in a silicon material to determine the spectrum by suitable signal processing. Secondary targets reduce background noise compared to the output signal from the tube and improve fluorescence detection. Liquid samples were placed in 6 mm diameter cups, the bases of which consisted of a 4 mm-thick proline film. The XRF spectrometer was used to analyse a series of eleven cups in sequence, using a rotating carousel that positions the samples to be measured above the inverted optical part. A volume of 200 µL of each of the samples was placed in the microcups for analysis for a duration of 40 min. The X-ray tube generator was set at 40 kV and an intensity of 0.160 mA. The zirconium secondary target was monitored between 15 and 17 keV to visualise the fluorescence of all lanthanides and between 4 keV and 10 keV for iron.

In order to quantify the elements from the raw spectra, we used a calibration procedure described and further detailed in the Supporting Information. In other words, one XRF spectrum yields a concentration value after processing with the calibration. Calibration was carried out using commercial ICP-OES standard solutions.

2.7. *Small- and wide-angle X-ray scattering (SWAXS) experiments*

Small- and wide-angle X-ray scattering experiments were carried out on a bench, built by Xenocs using X-ray radiation from a molybdenum source (λ = 0.71 Å), delivering a 1 mm-large circular beam of 17.4 keV. The scattered beam was recorded by a large on-line scanner detector (MAR Research 345) which was located 750 mm from the sample stage. Off-center detection was used to cover a large q range simultaneously ($0.2\ \text{nm}^{-1} < q < 30\ \text{nm}^{-1}$, $q = (4\pi/\lambda)\sin(\theta/2)$).

Collimation was applied using a 12:∞ multilayer Xenocs mirror (for Mo radiation), coupled to two sets of Forvis scatterless slits, which provides a 0.8 mm × 0.8 mm X-ray beam at the sample position. A high-density polyethylene sample (from Goodfellow) as

a calibration standard was used to obtain absolute intensities. Silver behenate in a sealed capillary was used as scattering vector calibration standard. Integration of the two-dimensional spectra was performed, using the FIT2D software. Data were normalised considering the electronic background of the detector, transmission measurements, and empty cell subtraction. The acquisition time was 1800 s per sample.

Fitting of the spectra was done with the SasView package [26], assuming two different models. On the one hand, an Ornstein–Zernike formula was used for composition fluctuations which gives information about the pseudo-phase domain size [27], on the other hand, a simple sphere model was used to fit mainly the spectra near the EA-rich region where little aggregates are observed. More detailed information can be found in the manual [26].

3. Results and discussion

3.1. *Conductivity experiments*

In order to investigate the structuring of the ternary mixtures H_2O/NaSal/EA, conductivity measurements were performed first. Conductivity measurements provide detailed information on the mobility of charge carriers and yield insight into the local structuring of a system [6,28–31]. Conductivity measurements in the domain of microemulsions are a common and very well-known method to distinguish between regions of w/o, o/w and bicontinuous microemulsions [24,32]. In order to obtain meaningful and conclusive results, the conductivity must be measured by diluting with water but also by diluting with the solvent (EA). In both cases, the polar fraction contains all the charge carriers.

Two different dilution lines (see the phase diagram on Figure 2a) as a function of α are depicted in Figure 2a. α is calculated in the investigated samples using the following equations:

$$\alpha = \frac{w_{\mathrm{EA}}}{w_{\mathrm{EA}} + w_{\mathrm{water}}} \tag{1}$$

where w_i is the weight fraction of molecule i in the ternary mixture.

It should be noted that the same alpha value can be obtained for two samples with different compositions (see Figure 2a). So, the reader is kindly invited to refer both to the alpha value but also to the color code of the graphs and dilution lines. The water dilution line is shown in blue and the solvent dilution line is shown in red.

In Figure 2a, the red curve shows a decrease in conductivity when α increases. At α values above 0.9, the polar volume fraction is too small to obtain significant conductivity values (a few $\mu S \cdot cm^{-1}$) but a flat rise in the conductivity with decreasing α values is observed (at low water content). Below 0.9, the charge carriers are released (increase in the polar fraction), and a linear increase in conductivity is observed. A strong linear increase in conductivity with increasing water content is observed followed by a change in slope at $\alpha = 0.4$. It should be noted that this slope change at ($\alpha = 0.4$) corresponds to the pre-nucleation cluster (PNC) region [22].

In order to determine the origin of the sharp increase in conductivity as well as for a better understanding of the curve shape, conductivity was normalised to the reduced equivalent conductivity. It should be noted that the conductivity depends on two critical factors:

- the concentration of charge carriers present in the solution
- the volume in which these charge carriers can move.

Thus, we normalised the experimentally determined specific conductivity σ and translated it to the reduced equivalent conductivity Λ^*, according to:

$$\Lambda^* = \frac{\sigma}{c(\mathrm{NaSal}) \cdot \phi^*_{\mathrm{polar}}} \tag{2}$$

where ϕ^*_{polar} is an estimation of the polar volume fraction taking into account the distribution coefficient of the three components. The polar volume fractions were calculated in the investigated samples using the following equation:

$$\phi_{\mathrm{Polar}} = 0.1 \cdot v_{\mathrm{EA}} + 0.96 \cdot v_{\mathrm{water}} + 0.9 \cdot v_{\mathrm{NaSal}} \tag{3}$$

where v_i is the volume fraction of molecule i in the ternary mixture.

We call Λ^* the "reduced conductivity" or "reduced equivalent conductivity" of the system, in order to avoid confusion with notations of the equivalent conductivity Λ. This normalisation is based on the conductivity introduced in the charge-fluctuation model presented by Eicke et al. [33], where the specific conductivity is normalised by the volume

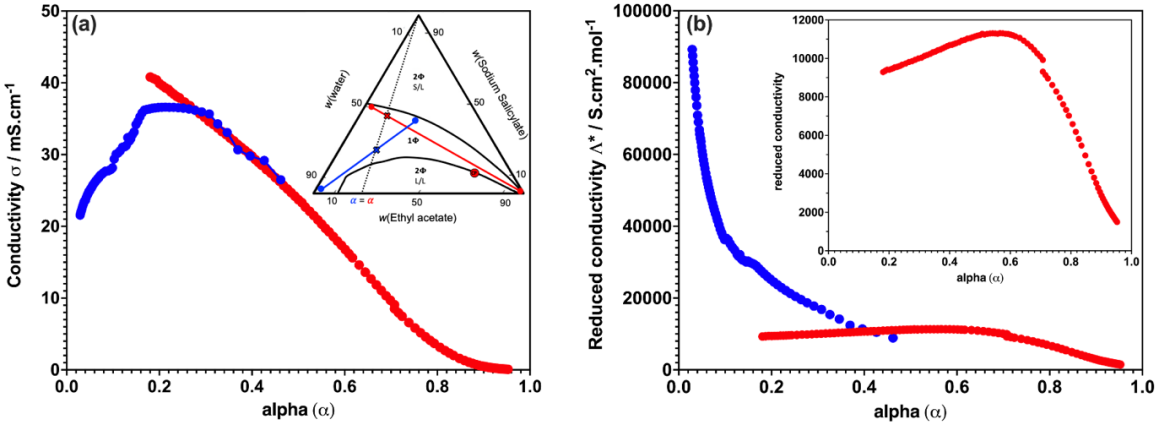

Figure 2. (a) Conductivity, (b) reduced conductivity measured along the two dilution lines represented in the phase diagram as a function of α that is the mass fraction of water versus ethyl acetate, not taking into account the mass of hydrotrope. The insert is a scaled-up graph of the reduced conductivity of the dilution line with ethyl acetate. The black dashed line on the phase diagram shows that two samples with different compositions (red and blue crosses) can have the same α value.

fraction of water. Further, the background to normalise the conductivity by the NaSal concentration stems from the classical aqueous model, which has also been adapted in one of Eicke's earlier works [28]. This reduced conductivity is thus the contribution of a single charge carrier to the total conductivity.

Figure 2b shows the reduced conductivity Λ^* as a function of α for the same two dilution lines depicted in the phase diagram. For α below 0.6, the reduced conductivity depends weakly on the amount of solvent present, i.e. the majority of mobile ions are free to move. The maximum of reduced conductivity occurs when charged PNCs are detected by their scattering pattern.

The conductivity of the dilution line towards water is shown in Figure 2a in blue. The curve is bell-shaped, characteristic of pre-Ouzo aggregates showing an increase towards low water contents [7]. With an increasing water content, a maximum is reached before the conductivity decreases again due to excessive dilution of the present charge carriers ($0 < \alpha < 0.2$). For the reduced conductivity, a slope change is observed below $\alpha = 0.1$, demonstrating the dissociation of the pre-Ouzo aggregates present near the phase boundary.

For $\alpha > 0.9$, the slope of reduced conductivity is smaller than in the water corner: charge carriers could be aggregates.

3.2. *NMR experiments*

Figure 3 shows the self-diffusion coefficients of the three molecules composing the ternary system: NaSal, EA, and water as a function of α. These self-diffusion coefficients allow us to see the interactions of each molecule with the others. The self-diffusion coefficients were measured along the two dilution lines (the numbered samples on the phase diagram, see Figure 3a).

Figure 3a shows the self-diffusion coefficient of NaSal along the two dilution lines. Starting from the EA-rich corner (red curve, $\alpha = 0.93$), we can see that in an organic medium, the NaSal molecule cannot move freely compared to the water-rich corner (blue curve, $\alpha \approx 0$), where NaSal is more mobile with a 50-fold increase in diffusion coefficient. This value decreases with the decrease in α (from sample 11 to 20 on the phase diagram, Figure 3a) passing through the PNC region, already discussed in a previous paper [1], and then towards the solid/liquid region where the value of D is minimal. For the water dilution line, the difference in diffusion coefficients between the two extremities of the curve (between sample 1 and 9) is more pronounced compared to the red dilution line (between sample 11 and 20) with a minimum reached near the PNC region ($\alpha = 0.4$). This indicates that the NaSal molecules (or their ions) are distributed between water and EA with a preference for

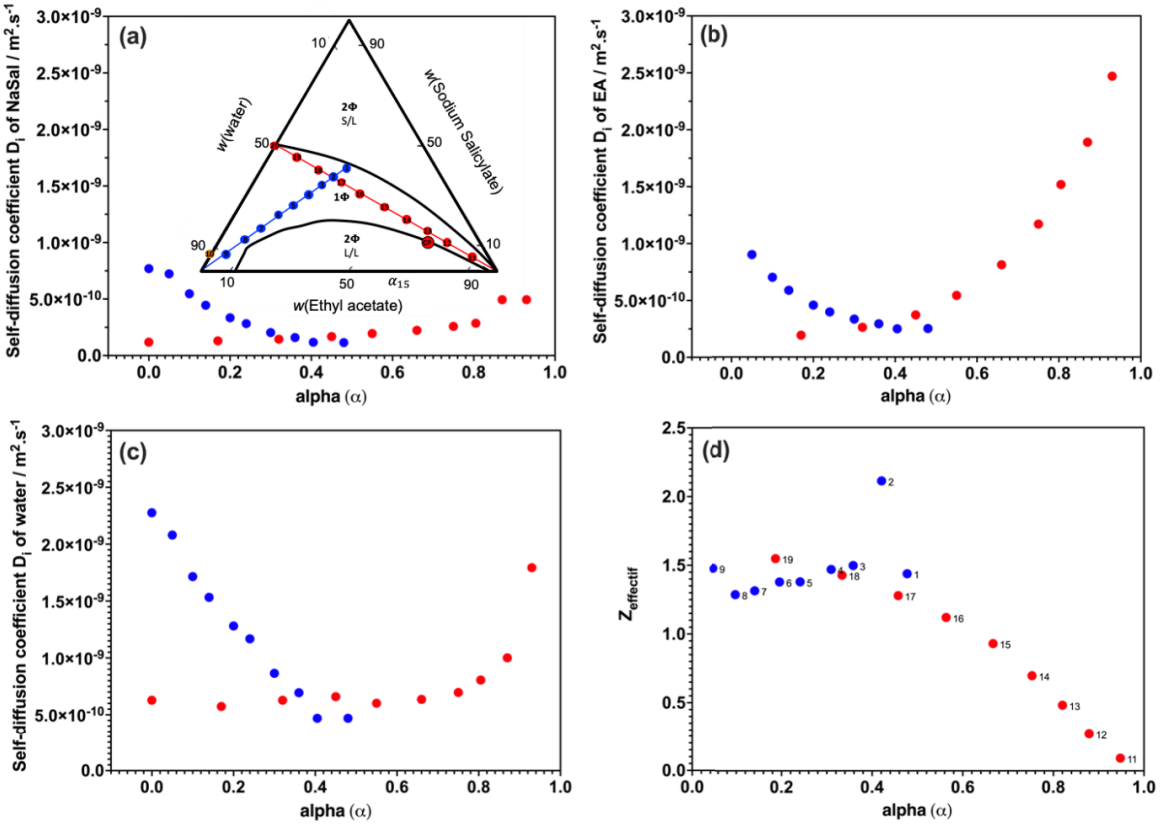

Figure 3. Self-diffusion coefficients as a function of the water/EA mass ratio α of (a) sodium salicylate, (b) ethyl acetate, (c) water, as well as (d) the effective charge derived from the ratio of conductivity to self-diffusion along the water (blue) and EA (red) dilution lines at the positions shown in the phase diagram.

water. This is consistent with the slope of tie-lines observed in the biphasic region and with the fact that ethyl acetate acts as a weak antisolvent. This is also in agreement with the results obtained in a previous publication concerning the same ternary system, where using optical density we noticed that in EA-saturated water (20 wt%), sodium salicylate micellises like a medium-chain classical surfactant [22].

Figure 3b and c represent the self-diffusion coefficients of EA and water, respectively. The trends are quite similar. In the EA-rich corner, the EA curve reaches its maximum (red curve, $\alpha = 0.93$) and then decreases exponentially with decreasing α passing by the PNC region and approaching the solid/liquid phase separation limit. In the blue dilution line, the D value of EA decreases with increasing α (from sample 9 to 1 on the phase diagram) and remains constant for $\alpha < 0.4$. For water and in the water-rich corner, the D values decrease considerably with increasing α until it reaches a constant value at $\alpha = 0.4$. Concerning the red curve, the D of water decreases from sample 20 to 11, but this decrease is not pronounced compared to the decrease of D of EA. It should be pointed out that in the PNC region, where the two dilution curves cross, we notice that NaSal and EA have approximately the same value of D. This is not the case for water, which confirms that the EA and NaSal molecules are confined in the same small aggregates and that water is the main component of the "external" solvent as already reported [22].

Figure 3d shows the effective charge as a function of α for each point where self-diffusion coefficients were measured. The effective charge Z was calculated assuming that NaSal is the only charge carrier according to the equation:

$$Z = \sqrt{\frac{kT\sigma}{e^2 DC}} \tag{4}$$

where k (joules per Kelvin) is the Boltzmann constant, T (Kelvin) is the temperature, σ (milliSiemens per centimetre) is the conductivity, e (coulombs) is the elementary charge, D is the self-diffusion coefficient in cm^2/s and C is the solute concentration in molecules per m^3.

In Figure 3d, we can see that the effective charge of the main charge carrier near the PNC as well as the pre-Ouzo region is above 1. Near the EA corner, NaSal is only partially dissociated or forms neutral clusters. The calculation of the effective charge gave us the approximate average charge in the pre-Ouzo region as well as in the PNC region. As these PNCs are negatively charged aggregates with a charge ranging from 1.5 to 2, we wondered what would happen if we added a trivalent ion (for example a lanthanum) to a ternary mixture of a given composition in the monophasic region.

3.3. *Solubilisation map*

Figure 4 shows the saturation concentration of lanthanum—converted to solubilisation efficiency (E%)—in the monophasic region as a function of the location in the phase diagram. The solubilisation experiments were performed in vials by adding lanthanum salt to a given ternary mixture. Different compositions of the ternary mixtures in the monophasic region were tested to obtain a mapping of solubilisation efficiency as shown in Figure 4. A stirring bar was added to the solution, and the lanthanum was added gradually to the solution until a solid/liquid separation occured, i.e., the solution was saturated with lanthanum. The vials were then closed with a sealed lid. The mixtures were stirred for 15 h at room temperature. Afterwards, the vials were centrifuged for 10 min at 5300 rpm. The concentrations were obtained after filtration of the solid residue and measurement of the remaining liquid by XRF. The solubilisation efficiency (E%) is defined as:

$$E\% = \frac{\text{Amount of metal in the solution}}{\text{Total amount of metal in the solution and residue}}. \quad (5)$$

As shown in Figure 4, we can distinguish four regions where the solubilisation of lanthanum, and consequently the saturation concentration are high.

(1) The region near the critical point, which is a classical critical point. No pre-transition effect due to heterophase fluctuation was observed. It is known that critical fluctuations can lead to a remarkable enhancement of the solubility [1,34,35]. The solubilisation regime in this region is governed by critical fluctuations and thus by entropy linked to concentration fluctuations of NaSal [36].
(2) The second region is the region previously called "pre-Ouzo" region which was observed first by conductivity measurements (and confirmed later by SAXS). These are dynamic aggregates in the water-rich region at the phase separation boundary.
(3) The third region with high solubilisation is the region where prenucleation clusters (PNC) are formed. As mentioned before, these PNCs with inter-aggregate distance of 2.5 nm possess an effective charge of 2. Thus, solubilisation in this case is mainly governed by electrostatic interactions between the charged aggregates and the trivalent lanthanum.
(4) And finally, a region close to the oil-rich corner. In this region, reverse aggregates coexist in equilibrium with monomers, and a more detailed study of this region will be the focus of the following part of this paper.

It has been shown in several studies that salicylate and lanthanides form stable complexes of different stoichiometry [37–41]. Aoyagi et al. reported a stability constant only for the 1:1 complex [38]. Hasegawa et al. determined the stability constants of complexes with 1:1 and 1:2 metal-to-ligand ratios and also thermodynamic data (but only the reaction enthalpy) of these two complexes in the case of europium only [42,43]. Irving and Sinha reported additionally the thermodynamic data of the neutral 1:3 complex $Eu(Sal)_3$, detected with solvent extraction [39]. A crystal structure of the 1:3 complex was published by Kuke et al. [37]. However, in solution they assume the existence of only the 1:1 and 1:2 complexes. Also, a theoretical study concerning possible structures of the 1:1 complex in an aqueous phase has been published [40]. Wujuan et al. have studied a series of rare earth complexes using different spectroscopy techniques. They demonstrate that the lanthanide ions coordinate with salicylate via the carboxyl group. They also showed that energy transfer between the salicylate and the rare-earth ions is the primary process and that the heavier the rare

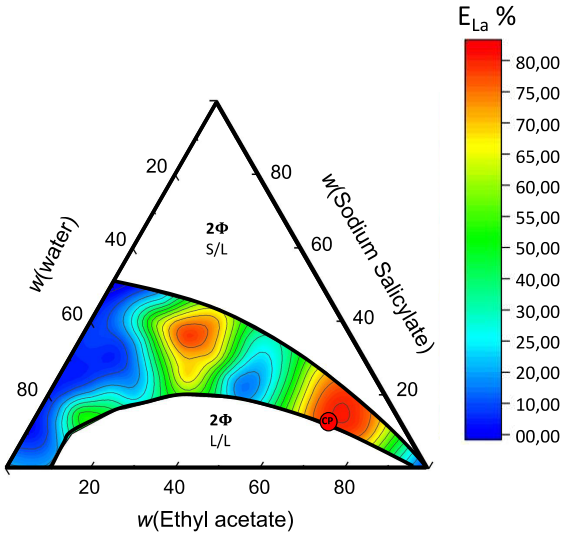

Figure 4. Solubilisation map of lanthanum in the water/NaSal/EA ternary system. The colour scale relates to a relative value of solubilised lanthanum nitrate observed in the presence of a small excess of solute.

earth, the higher the efficiency of intermolecular energy transfer [44].

However, these four solubilisation regimes cannot be explained with only a complexation mechanism between lanthanum and salicylate. If this was the case, there should be a correlation between the solubilisation efficiency and the amount of NaSal in the ternary solution. In other words, a better solubilisation with high quantities of NaSal could be expected since there will be more free sites to complex the lanthanum. On the other hand, a sharp decrease should occur when the ternary mixture contains less NaSal, i.e., less complexing sites. This correlation between the amount of NaSal and solubilisation is not observed and we can reach E% values higher than 50% even with small amounts of NaSal in the region called pre-Ouzo and the EA-rich region (see Figure 4). To understand the origin of these solubilisation regimes, we investigated the structuring of these ternary systems using scattering techniques. The aim was to see if there is a solubilisation–structure relationship that can explain these observed regimes.

It should be noted that theses solubilisation regimes were not found in the case of curcumin solubilisation, which is effective only near the critical point [45]. This is maybe due to the fact that curcumin is a large uncharged molecule and thus difficult to solubilise compared to rare-earth salts which are electrolytes involving a first layer of highly bound solvating water molecules ($V_{\text{curcumin}} = 4.701 \times 10^2$ Å^3 > $V_{\text{lanthanum}} = 3.757 \times 10^1$ Å^3).

The solubilisation of lanthanum salts was investigated in the monophasic region above the liquid/liquid miscibility gap of the ternary system. Whenever solubilisation is efficient near a liquid/liquid miscibility gap, separation and purification processes in the biphasic region can be performed via liquid/liquid equilibria, which will be the focus of a next paper.

3.4. *Small-angle X-ray scattering (SAXS) of ternary mixtures and microstructures inferred from them*

To better understand the link between solubilisation and microstructure, SWAXS experiments were carried out on the different regions where lanthanum solubility was at its maximum.

The primary subject of this study was a detailed characterisation of the microstructures in the monophasic region of the water/NaSal/EA system. X-ray techniques are among the few suited methods for probing structure transitions. SWAXS is particularly appropriate, as it gives multiscale information from atomic scale up to colloidal scale. In previous work, investigations of microstructures in ternary mixtures of the considered water/NaSal/EA system focused only on the so-called "Pre-Nucleation Cluster" region near the solid/liquid boundary. The current work aims to cover the entire monophasic region of the phase diagram in order to understand the relationship between the solubilisation of trivalent ions and the microstructure. The samples chosen are illustrated in Figure 5 with the corresponding SWAXS spectra.

In order to determine the correlation length and the radii of the aggregates, an Ornstein–Zernike (OZ) formalism was used for data fitting in the low-q range (0.2–4 nm^{-1}). The OZ function can be converted into an effective radius of gyration R_G of the aggregates by:

$$I(q) = \frac{I_0}{1+\xi^2 q^2} = \frac{I_0}{1+\frac{R_G^2 q^2}{3}} \qquad (6)$$

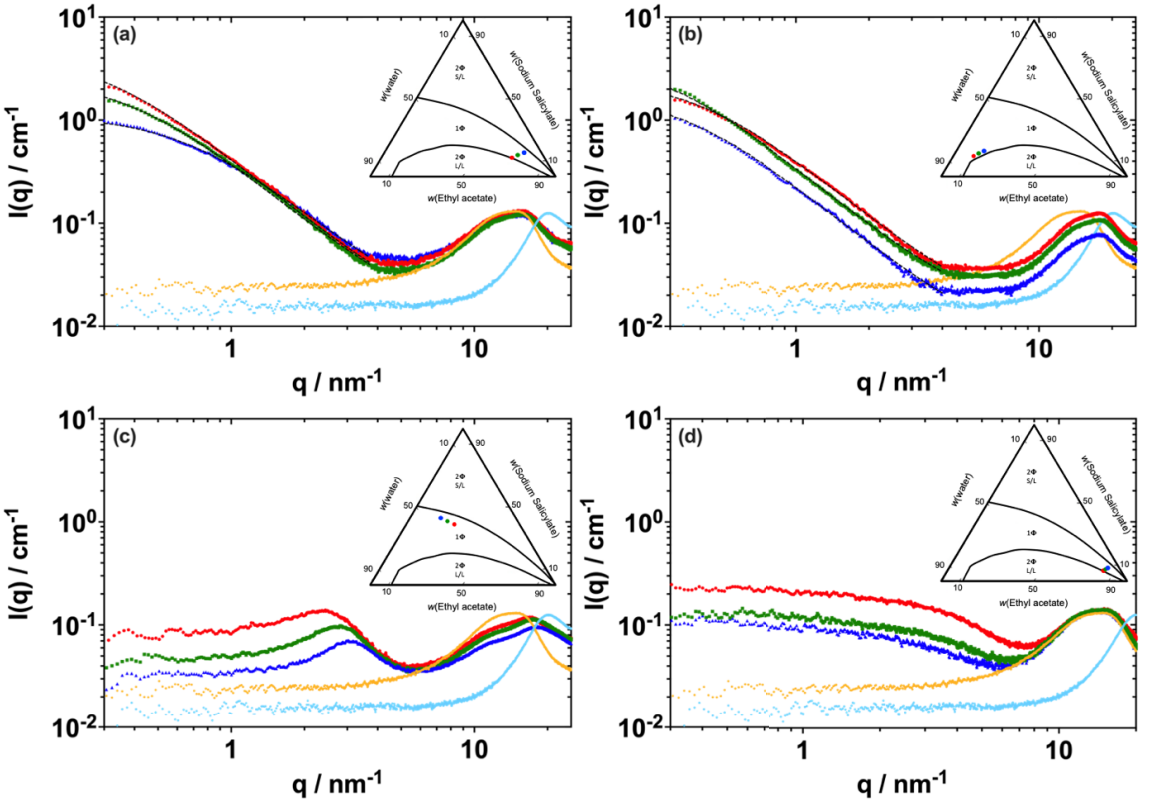

Figure 5. Experimental small and wide angle X-ray scattering (SWAXS° curves and their corresponding location on the phase diagram for: (a) the region near the critical point, (b) the region of pre-Ouzo aggregates, (c) the region of pre-nucleation clusters (PNC), i.e., ternary aggregates involving typically 6 to 20 EA molecules associated with NaSal and water, and (d) the region of weak reverse w/o aggregates. In the four figures, the light blue spectrum corresponds to pure water, while the orange one corresponds to pure EA for comparison. Figure (a) is dominated by critical scattering, Figure (b) by OZ behaviour far from the critical point corresponding to polydisperse surfactant-free microemulsions (SFME), while Figure (d) is typical scattering from supramolecular stoichiometric complexes.

where ξ is the correlation length and I_0 the intensity for $q = 0$. The spherical radius R_S of all identical compact spherical aggregates stands as:

$$R_G^2 = \frac{3}{5} R_S^2. \tag{7}$$

In this case, the link between correlation length and the spherical radius of the aggregate is valid:

$$R_S = 2.24 \cdot \xi. \tag{8}$$

In Figure 5a, different SWAXS experimental spectra are shown in log–log scale for the critical point as well as for pure water and pure EA. The colour of each of the spectra corresponds to the colour of the sample presented in the associated phase diagram. In the WAXS regime, above 7 nm^{-1}, the curves converge and a peak is visible. This broad peak is linked to different packings of aliphatic chains. We have not observed any peak linked to crystallinity [46]. In the small-angle regime below 7 nm^{-1}, all spectra show an intense OZ signal ($I_0 > 1$ cm^{-1}) which weakens with the distance from the critical point. Table 1 shows the values of the correlation length (ξ) as well as the radius of the aggregates (R_S), which effectively decreases from ξ = 32 Å to ξ = 14.5 Å. This means that critical fluctuations persist event far from the critical point (dark blue sample on Figure 5a). This confirms that critical fluctuations, driven by entropy, govern the solubilisation

Table 1. Structural parameters obtained from fitting the spectra near the critical point as well as those in the pre-Ouzo region

	Critical point region			Pre-Ouzo region		
	Red sample	Green sample	Blue sample	Red sample	Green sample	Blue sample
Forward scattering I_0 (cm^{-1})	4.53	2.65	1.13	2.6	4.2	1.88
Correlation length (Å)	32	25	14.5	25	35	29
Background (cm^{-1})	0.01	0.01	0.01	0.015	0.014	0.01
R_S	71.68	56	32.48	56	78.4	64.96

regime in this region as already mentioned (see Figure 4).

In Figure 5b, SWAXS experiments are performed in the second region, where solubilisation of lanthanum is maximal, called "pre-Ouzo region". As in Figure 5a, the curves converge in the WAXS regime above 7 nm^{-1}. While the WAXS local correlation peak of ethyl acetate can be found around 14 nm^{-1}, the signature peak of water is located at 20 nm^{-1} (the spectra of the pure solvents are plotted in each case of Figure 5 (the light blue spectrum is for water and the orange one is for ethyl acetate). The position of the peaks in Figure 5b are slightly shifted towards higher q values (q = 17.9 nm^{-1}), due to higher water content compared to the samples of Figure 5a, where the opposite was found. Indeed, the peak remains at q = 14 nm^{-1} due to the low amount of water in the ternary solution. Diat et al. have shown that the WAXS signal for mixtures of three solvents can be approximately estimated by superposition of the pure solvent spectra [10]. At low q values ($q < 7$ nm^{-1}), a strong OZ behaviour is also observed even far from the critical point, as it is expected in the case of heterophase fluctuation due to pre-transition effects called pre-Ouzo effect previously [47]. These signals indicate the formation of dynamic aggregates at the nanometre scale. To estimate the size of these aggregates, the Ornstein–Zernike equation was applied (see Equation (6)). We obtained a value I_0 between 1.88 and 4.2 cm^{-1} for the zero-angle intensity, and a value of ξ between 25 and 35 Å for the correlation length, which is a measure for the size of the aggregates. Thess results prove the presence of mesoscopic objects, which are larger than in the case of the well-studied water/ethanol/1-octanol system [3,48,49]. This difference in correlation lengths is related to the miscibility of water in ethyl acetate that is larger than in 1-octanol [50].

In Figure 5c, SWAXS spectra are shown for the third solubilisation region, which is the pre-nucleation clusters (PNC) region. The spectra in this region show a particular forward scattering behaviour: a broad peak corresponding to a distance in real space derived from the peak position of 2 nm is detected. This result is in good agreement with reports in the previous work of El Maangar et al. which was devoted to this PNC region [22]. Using SWAXS and small angle neutron scattering (SANS) measurements, the presence of aggregates was confirmed, with an inter-aggregate distance of 2 nm in a region where density anomalies were observed. These PNC aggregates contain 12 NaSal molecules and a mole ratio of 1 NaSal to 2 EA inside the aggregates [22]. Their effective average charge is 2 (see Figure 3d) corresponding to a dissociation of approximately 16% of the sodium salt included in a PNC, which is consistent with the dressed model of micelles [51]. Thus, it can be concluded that solubilisation in this domain is dominated by electrostatic interactions between negatively charged aggregates with a surface charge of 0.15 e/nm^2 and trivalent cations.

Figure 5d shows the SWAXS spectra of the fourth solubilisation domain in the EA-rich region. In the WAXS regime, the curves converge, and a peak is visible at q = 14 nm^{-1}, which corresponds to the peak of pure EA. This is due to the low amount of water in this region and already observed in the case of the critical fluctuation region (cf. Figure 5a). At low q values, a signal close to what is observed for the well-described weak w/o aggregates is measured [52]. The scattering intensity at low q values increases only slightly (I_0 = 0.2) when approaching

the phase boundary. The intensity values at low q are within the range of a ternary solution that contains weak aggregates.

These spectra show an organisation of NaSal molecules in EA. Indeed, with the addition of water to the "blue" sample, an increase at small angles appears which is more marked for the "red" sample than for the "green" sample. The increase in intensity indicates that the aggregation of salicylates is favoured by the addition of water, which favours the organisation of small inverse aggregates of salicylate molecules. These aggregates are therefore either more numerous or larger with the addition of water. The effect of water on the size of the aggregates' polar core has already been studied in the case of aggregates of extractants like DMDOHEMA for example [53]. It has been shown that the amount of water co-extracted in the polar core of the w/o reverse aggregates of extractants influences their size and thus the extraction performances, since more ions in the core require a higher dilution in order to reach a stable form. The water extraction and its influence on stabilisation of the aggregate core are often reported in the literature [54–57]. These results prove the presence of small w/o inverse aggregates in the EA-rich side, which are more stable with the addition of water. These results are in perfect agreement with the previous work of El Maangar et al. where they found by using optical density measurements of added DR-13 dye that NaSal already starts to "micellise" in the presence of water saturated with ethyl acetate much as a medium-chain classical surfactant. This confirms the antisolvent effect of ethyl acetate for NaSal [22].

In this case, form factors, modified by a Baxter interaction term if necessary, are more suited than an OZ fit in absolute scale. The form factor $P(q)$ was taken as a simple sphere without attraction, since there is no hard sphere effect when aggregates are produced by fluctuation. Details of equation are given in the Supplementary Material. $P(q)$ depends on the aggregates' radii and their scattering length density. The latter was estimated by taking into account the "lowest aggregation concentration" (LAC) of NaSal, which corresponds to the concentration of monomers in equilibrium with the aggregates as well as the solubility of water in EA. Details of calculation and estimated values are also shown in the Supplementary Material.

Overall, all the quantities are fixed thanks to the sample composition already determined, and the only variable is the aggregation number N_{agg}.

Figure 6 shows the experimental spectrum (same as the red one in Figure 5d) as well as the calculated spectra for different aggregation numbers $2 < N_{agg} < 10$. Imposing a priori histograms of aggregates size would require too many parameters [3]. In binary systems, an approximation is usually made: an aggregate of N molecules produces a form factor with N times the molecular volume. We have extended this approximation to ternary systems with the known water-to-NaSal ratio for each sample. The multiple-equilibria model requires that aggregates of N_{agg} molecules must coexist with aggregates of $N_{agg} - 1$ and $N_{agg} + 1$ [58]. The size distribution function depends on the exact form of the free energy linked to stacking or packing and cannot be derived quantitatively. Figure 6 shows the calculated spectra for monodisperse aggregates from $N_{agg} = 2$ to $N_{agg} = 10$ as well as the spectrum that best fits the experimental result. This spectrum I_{cal} is obtained by minimising the following equation:

$$I_{cal} - I_{exp} = 0 \tag{9}$$

with:

$$I_{cal}(q) = \sum_{N_{agg}=2}^{N_{agg}=10} x_{N_{agg}} \cdot I_{N_{agg}}(q) \tag{10}$$

$x_{N_{agg}}$ is the proportion of aggregates with N_{agg} NaSal molecules in the sample, and $I_{N_{agg}}(q)$ is the calculated spectrum for monodisperse aggregates with an aggregation number of N_{agg}.

The result of this equation shows that the sample contains mainly aggregates with $N_{agg} < 5$, and the tetramers (i.e., aggregates of four NaSal molecules) are the dominant species. So they are indeed small w/o aggregates with an aggregation number below 5.

To conclude the first part of this work, the experimental analysis allowed us to confirm that four solubilisation regimes exist in the monophasic region. Furthermore, SWAXS measurements give proof that these four regimes correspond to four different microstructures: pre-nucleation clusters (PNC), critical fluctuations (CF), direct pre-Ouzo aggregates (PO), and reverse aggregates (RA). This allows us to define a mapping of the monophasic domain as depicted in Figure 7. Note that, in addition to the data shown here, other compositions were investigated with the

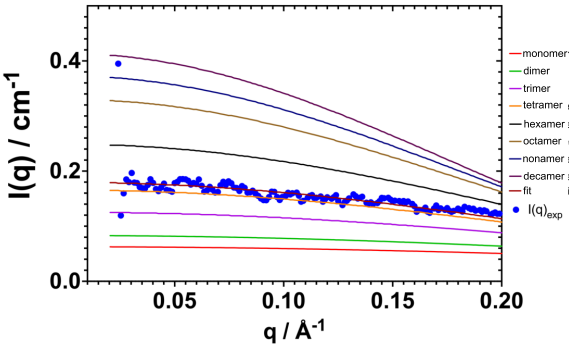

Figure 6. Experimental and theoretical Small Angle X-ray Scattering (SAXS) curves for the complexes formed in the EA-rich region represented in logarithmic scale.

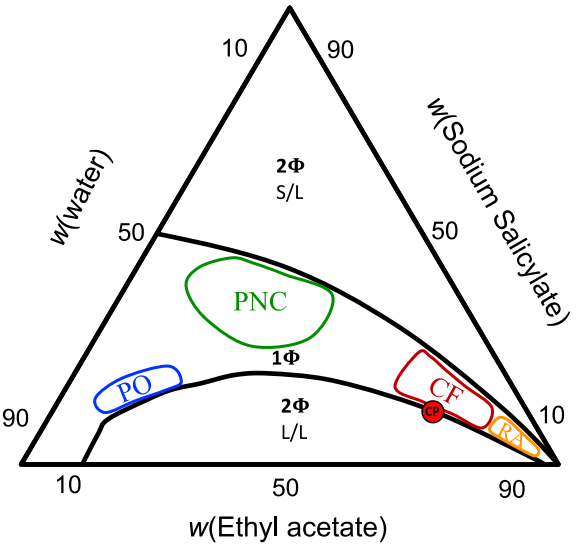

Figure 7. Schematic view of the mesoscopic structuring in the ternary phase diagram water/NaSal/EA. The region around the liquid/liquid phase transition border is dominated by three different regimes: the regime where pre-Ouzo aggregates are dominant (PO), critical fluctuations (CF) and supramolecular complexes (RA) are close to the L/L miscibility gap while pre-nucleation clusters (PNC) are close to the solid/liquid phase separation boundary, while one further regime exists near the solid/liquid phase boundary. The white monophasic region corresponds to a simple molecular solution.

help of SWAXS experiments. The results and discussion of these data are given in Figures S1 and S2.

3.5. *Effect of lanthanum salt on miscibility gap and tie-lines*

A striking observation is the shift in the liquid/liquid phase boundary of the miscibility gap and a variation of the slope of tie-lines when adding lanthanum salt to water. A similar effect was initially observed by Tobias and coworkers when adding sulfuric acid to the water/ethanol/1-octanol ternary system [48].

As shown in Figure 8, the monophasic region is growing slightly on the water-rich side of the phase diagram with increasing concentration of lanthanum salt, ranging from 0 to 100 mM. By contrast, the biphasic region grows in the EA-rich side. There is a crossing of the binodals reflecting the change in partition of the hydrotrope (NaSal). The critical point is experimentally identical to the point marked in red for low concentrations of lanthanum.

The maximum amount of added NaSal is reduced from 20 wt% for pure water to 16 wt% for aqueous solutions containing 30 mM of lanthanum salt. The increase seems to be proportional to lanthanum salt concentration.

Considering the different types of mesoscale structuring introduced in the first part of this work, the lanthanum salt stabilises the pre-Ouzo aggregates, while it reduces the region where critical fluctuations and w/o tetramers are observed. Addition of electrolytes reduce the stability of w/o aggregates regardless of the electrolyte considered. This is due to the Born energy of the electrolyte in EA [59].

The displacement to the right of the binodal lines is thus the result of two opposing features: the additional stabilisation (salting in) in the water-rich region and the salting out of water out of ethyl acetate in the EA-rich region. The partition of NaSal is significantly shifted towards a higher NaSal concentration in the aqueous phase. This can be seen by the change in the slope of the tie-lines, as represented in Figure 9.

To check whether the four different regimes are still present after addition of lanthanum salt or if they experience serious structural rearrangements, SWAXS spectra have been recorded in each of the four regimes. The compositions corresponding to

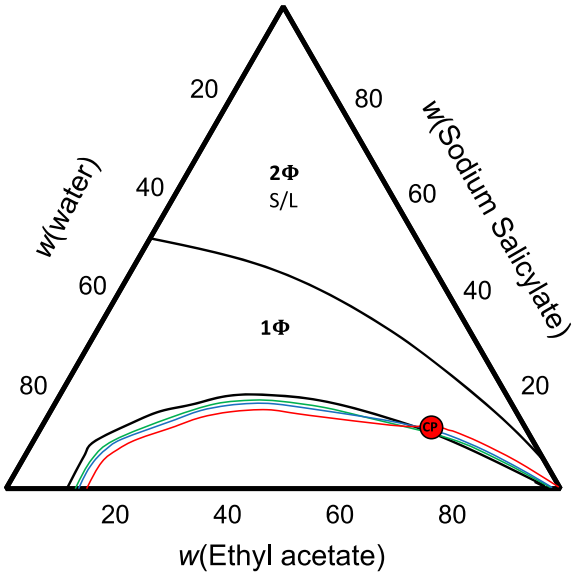

Figure 8. Phase diagram of EA/NaSal/aqueous solution of lanthanum. The phase diagrams are plotted in weight fractions wt%. The boundary in black is without lanthanum nitrate; 0.01, 0.05 and 0.1 mol·L^{-1} are shown in green, blue and red respectively. Rare-earth salts produce salting-in on the water-rich side and salting out on the EA-rich side of the phase boundary while the critical point remains indifferent to the addition of rare-earth nitrate.

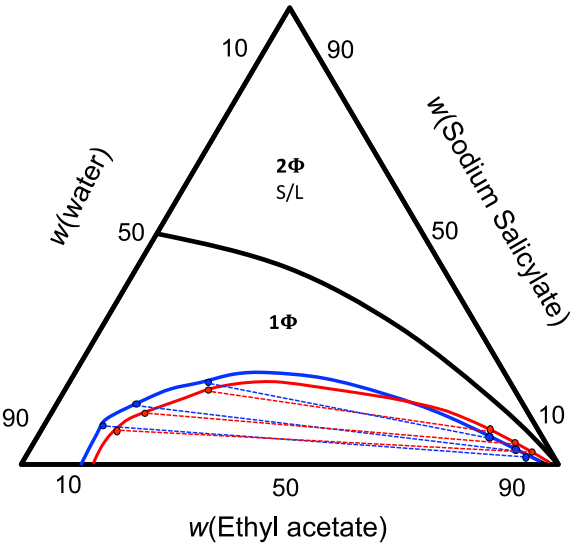

Figure 9. Pseudo-ternary phase diagram of lanthanum aqueous phase/NaSal/EA in wt%. The phase transition is given in blue for pure water, in red for 0.1 mol/L of lanthanum salt. Three tie-lines are given for each case: tie-lines rotate counterclockwise around the critical point that remains invariant in position.

the investigated samples are shown in the phase diagrams depicted in Figure 10, where the amount of water (in wt%) is replaced by the same amount of an aqueous solution of lanthanum (also in wt%). It should be noted that the significant amount of salt slightly changes the sample density, which would lead to different points in diagrams based on volume or mole fractions. As depicted in Figure 10, the shape of the spectra remains roughly the same and thus confirms that the aggregates are still present up to 30 mM of lanthanum salt. All spectra have a higher intensity in the low-angle scattering regime, except in the critical fluctuation regime, compared to the ternary systems without lanthanum salt. The introduction of an electron-dense component enhances the scattering contrast, which leads to an increase in intensity.

Figure 10a shows the SAXS spectra obtained near the critical point with and without lanthanum salt. The darkest red indicates the spectrum without lanthanum salt and the lighter shades the spectra at growing lanthanum concentrations in the aqueous phase. The addition of 0.1 M of lanthanum salt corresponds to an average distance between trivalent cations of 4 Å. Any fluctuation of more than 4 Å is quenched, because it implies modification of the distance between highly repulsive charged ions (0.105 nm). The location of the critical point is not noticeably changed, since it corresponds to the fluctuation concentration of NaSal.

Figure 10b shows that the main dominant aggregates are tetramers with or without lanthanum salt. The presence of trivalent salts increases the number of aggregates and reduces the critical micelle concentration (CMC). Attraction between the aggregates' cores is responsible for the smaller domain of stability [52].

Figure 10c shows that adding lanthanides in the PNC region (1 trivalent cation per cluster) produces an increase in cluster volume since the composition is the same. In the absence of lanthanum, the cluster contains 12 NaSal molecule, and the average

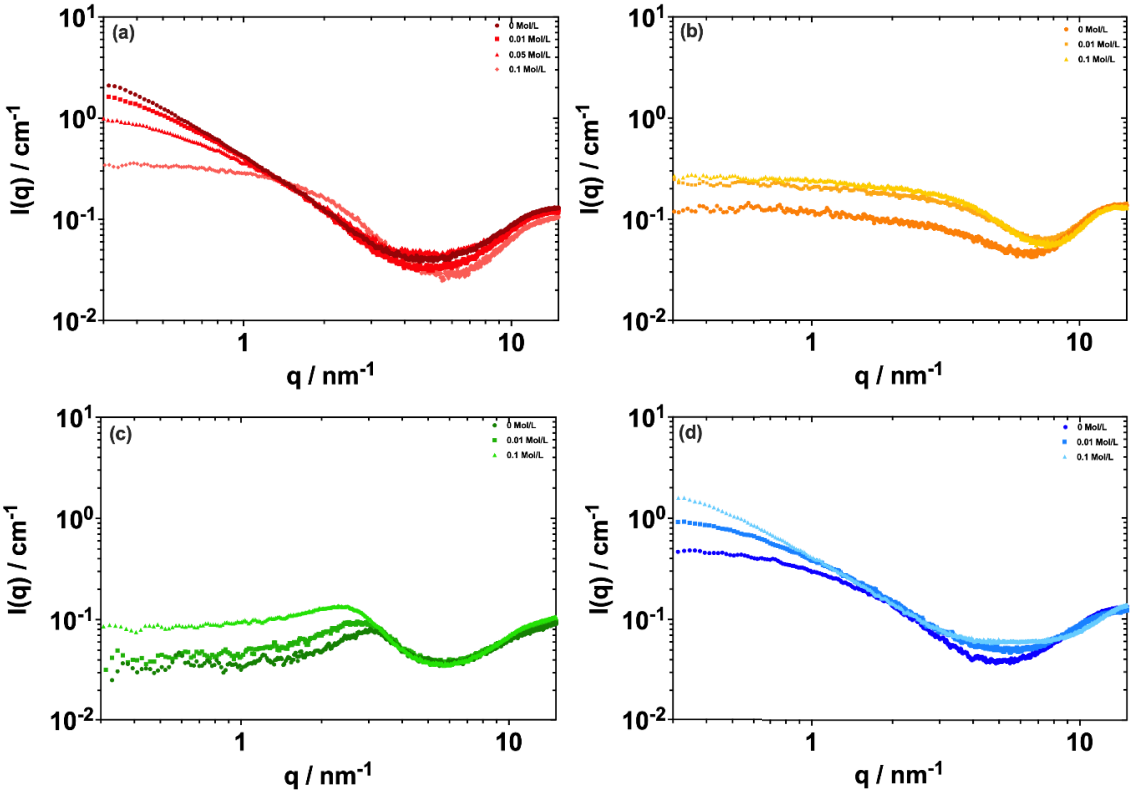

Figure 10. SWAXS spectra in the presence of lanthanum salt in the four solubilisation regimes: (a) critical fluctuations, (b) w/o reverse aggregates, (c) pre-nucleation clusters (PNCs) and (d) pre-Ouzo aggregates dominant in the scattering patterns.

distance between clusters is 2 nm. The addition of lanthanum produces a shift of the peak to the left and a corresponding distance of 2.5 nm between the clusters. Therefore, the average aggregation number increases from 12 to 24. The electrostatic interaction between the trivalent cation and monovalent salicylate favours larger PNC aggregates. This explains the high efficiency of solubility in this region.

Figure 10d shows that in the pre-Ouzo region, the correlation length increases when adding lanthanum salt. Lanthanum salts favour large pre-Ouzo aggregates. Values of correlation length are shown in the Supplementary Material. As in the case of the PNCs, this is a molecular mechanism responsible for the higher solubility in this domain. In between the PNC and pre-Ouzo domain, there is no local structuring that can be stabilised by lanthanide salts: this is the origin of the minimum of solubilisation observed between the pre-Ouzo and PNC region in Figure 4.

So far, we have only focused on lanthanum as a trivalent ion. However, for a future application, selectivity is a key parameter to implement a separation process. The solubilisation of four other rare-earths salts in addition to lanthanum nitrate was investigated in the two regions where solubilisation is maximal (see Figure 4), i.e., in the PNC and CF region. The results are summarised in Table 2. It can be seen that this ionic hydrotrope-based system can solubilise both light and heavy rare earths. A very slight selectivity is observed in the case of solubilisation in the region close to the critical point. This selectivity increases significantly in the PNC region. This is related to the solubilisation mechanism. In contrast to PNCs, the critical fluctuations do not induce differences between the solubility of ions, because the solubilisation mechanism is governed by entropy, which is not the case in the PNC region, where interactions between molecules are involved.

Table 2. Solubilisation efficiency of rare-earths elements

Sample	Solubilisation efficiency				
	$\%E_{La}$	$\%E_{Nd}$	$\%E_{Eu}$	$\%E_{Dy}$	$\%E_{Yb}$
PNC	73.6	80.9	91.4	95.2	97.1
CF	80.1	81.9	80.3	84.1	86.7

These results strengthen the interest of this eco-compatible system which can solubilise rare earths and in addition induce selectivity as well.

4. Conclusion

The solubilisation–structuring relationship in the monophasic region of the water/NaSal/EA ternary system was investigated. By performing conductivity, DOSY, SWAXS, and XRF measurements on different monophasic mixtures, we revealed fundamental changes in the nanostructuring of the system considered.

Four differently structured regions were detected and could be related to increased solubilisation regimes:

- Region CF is a region dominated by critical fluctuations, where entropy is the dominant driving force. In this region, the presence of trivalent ions quenches critical fluctuations.
- Region PNC containing pre-nucleation clusters, where charged aggregates of typically 12 EA molecules exist. In this case, solubilisation of rare-earth salts is enhanced by surface electrostatics of the prenucleation clusters and lanthanides increase their aggregation number.
- Region PO far from the critical point where small dynamic pre-Ouzo aggregates are present on the water-rich phase separation boundary. The aggregates in this region increase in volume upon solubilisation of rare-earth salts facilitated by the PO aggregates (also known as SFME or even UFME for ultra-flexible microemulsions). This mechanism is also known as mesoscale solubilisation.
- The diluted region on the EA-rich side, where reverse aggregates consisting mainly of tetramers coexist with monomers. The presence of lanthanides in this case increases the number of aggregates present, transforming them in supramolecular complexes. This is the only region for which the standard theory, taking only into account the complexation Gibbs energy difference combined with the mass action law, applies quantitatively. This complexation was the only theory for liquid/liquid extraction before the availability of the *ienaics* theory.

These different structure–solubilisation regimes and their modifications in the presence of electrolytes may have significant consequences on various applications [60]. The selectivity induced by this system may lead to a potential application in the field of rare-earth recovery, but this will be the topic of future research.

Declaration of interests

The authors do not work for, advise, own shares in, or receive funds from any organization that could benefit from this article, and have declared no affiliations other than their research organizations.

Acknowledgements

We thankfully acknowledge the CNRS for financial support through the International Research Project "NISI" program. JG thanks the Fonds der Chemischen Industrie for funding. We thank M.-H. Hengé for critical proof-reading of the manuscript.

Supplementary data

Supporting information for this article is available on the journal's website under https://doi.org/10.5802/crchim.310 or from the author.

References

[1] M. L. Klossek, D. Touraud, T. Zemb and W. Kunz, "Structure and solubility in surfactant-free microemulsions", *ChemPhysChem.* **13** (2012), pp. 4116–4119.

[2] V. Fischer, J. Marcus, D. Touraud, O. Diat and W. Kunz, "Toward surfactant-free and water-free microemulsions", *J. Colloid Interface Sci.* **453** (2015), pp. 186–193.

[3] S. Schöttl, J. Marcus, O. Diat, D. Touraud, W. Kunz, T. Zemb and D. Horinek, "Emergence of surfactant-free micelles from ternary solutions", *Chem. Sci.* **5** (2014), pp. 2949–2954.

[4] W. Kunz, K. Holmberg and T. Zemb, "Hydrotropes", *Curr. Opin. Colloid Interface Sci.* **22** (2016), pp. 99–107.

[5] K. Holmberg, D. O. Shah and M. J. Schwuger (eds.), *Handbook of Applied Surface and Colloid Chemistry*, Wiley: Chichester, England; New York, 2002.

[6] P. Bošković, V. Sokol, T. Zemb, D. Touraud and W. Kunz, "Weak micelle-like aggregation in ternary liquid mixtures as revealed by conductivity, surface tension, and light scattering", *J. Phys. Chem. B* **119** (2015), pp. 9933–9939.

[7] T. Buchecker, S. Krickl, R. Winkler, I. Grillo, P. Bauduin, D. Touraud, A. Pfitzner and W. Kunz, "The impact of the structuring of hydrotropes in water on the mesoscale solubilisation of a third hydrophobic component", *Phys. Chem. Chem. Phys.* **19** (2017), pp. 1806–1816.

[8] C. Neuberg, "Hydrotropische Erscheinungen", *Biochem. Z.* **76** (1916), pp. 107–158.

[9] J. Mehringer and W. Kunz, "Carl Neuberg's hydrotropic appearances (1916)", *Adv. Colloid Interface Sci.* **294** (2021), article no. 102476.

[10] O. Diat, M. L. Klossek, D. Touraud, B. Deme, I. Grillo, W. Kunz and T. Zemb, "Octanol-rich and water-rich domains in dynamic equilibrium in the pre-ouzo region of ternary systems containing a hydrotrope", *J. Appl. Crystallogr.* **46** (2013), pp. 1665–1669.

[11] P. Bauduin, A. Renoncourt, A. Kopf, D. Touraud and W. Kunz, "Unified concept of solubilization in water by hydrotropes and cosolvents", *Langmuir* **21** (2005), pp. 6769–6775.

[12] T. Zemb and W. Kunz, "Weak aggregation: State of the art, expectations and open questions", *Curr. Opin. Colloid Interface Sci.* **22** (2016), pp. 113–119.

[13] J. J. Booth, S. Abbott and S. Shimizu, "Mechanism of hydrophobic drug solubilization by small molecule hydrotropes", *J. Phys. Chem. B* **116** (2012), pp. 14915–14921.

[14] J. J. Booth, M. Omar, S. Abbott and S. Shimizu, "Hydrotrope accumulation around the drug: the driving force for solubilization and minimum hydrotrope concentration for nicotinamide and urea", *Phys. Chem. Chem. Phys.* **17** (2015), pp. 8028–8037.

[15] M. Špadina, K. Bohinc, T. Zemb and J.-F. Dufrêche, "Synergistic solvent extraction is driven by entropy", *ACS Nano.* **13** (2019), pp. 13745–13758.

[16] S. T. Kumar, D. G. Prakash and N. Nagendra Gandhi, "Effect of hydrotropes on solubility and mass transfer coefficient of lauric acid", *Korean J. Chem. Eng.* **26** (2009), pp. 1328–1333.

[17] Y. P. Koparkar and V. G. Gaikar, "Solubility of o-/p-hydroxyacetophenones in aqueous solutions of sodium alkyl benzene sulfonate hydrotropes", *J. Chem. Eng. Data.* **49** (2004), pp. 800–803.

[18] S. Theneshkumar, D. Gnanaprakash and N. Nagendra Gandhi, "Enhancement of solubility and mass transfer coefficient of salicylic acid through hydrotropy", *J. Zhejiang Univ. Sci. A* **10** (2009), pp. 739–745.

[19] R. Revathi, T. Ethiraj, V. S. Saravanan, V. Ganeshan, V. Saranya and T. Sengottuvel, "New spectroscopic determination of nifedipine using hydrotropic solubilization", *Int. J. Pharm. Pharm. Sci.* **2** (2010), pp. 74–76.

[20] K. Nidhi, S. Indrajeet, M. Khushboo, K. Gauri and D. J. Sen, "Hydrotropy: A promising tool for solubility enhancement: A review", *Int. J. Drug Dev. Res.* **3** (2011), pp. 26–33.

[21] E. Merinville, A. J. Byrne, A. V. Rawlings, A. J. Muggleton and A. C. Laloeuf, "Original contribution: Three clinical studies showing the anti-aging benefits of sodium salicylate in human skin", *J. Cosmet. Dermatol.* **9** (2010), pp. 174–184.

[22] A. El Maangar, P. Degot, V. Huber, J. Causse, P. Berthault, D. Touraud, W. Kunz and T. Zemb, "Pre-nucleation cluster formation upon ethyl acetate addition to an aqueous solution of an anionic hydrotrope", *J. Mol. Liq.* **310** (2020), article no. 113240.

[23] D. Gebauer, M. Kellermeier, J. D. Gale, L. Bergström and H. Cölfen, "Pre-nucleation clusters as solute precursors in crystallisation", *Chem. Soc. Rev.* **43** (2014), pp. 2348–2371.

[24] M. Clausse, L. Nicolas-Morgantini, A. Zradba and D. Tourand, *Microemulsion Systems* (H. Rosano and M. Clausse, eds.), Surfactant series, vol 24, CRC Press: Boca Raton, 1987.

[25] A. Jerschow and N. Müller, "Suppression of convection artifacts in stimulated-echo diffusion experiments. Double-stimulated-echo experiments", *J. Magnet. Res.* **125** (1997), pp. 372–375.

[26] M. Doucet, J. H. Cho, G. Alina, et al., *SasView version 4.1, Zenodo*, 2017. Online at http://www.sasview.org (accessed on May 20, 2019).

[27] S. Prevost, T. Lopian, M. Pleines, O. Diat and T. Zemb, "Small-angle scattering and morphologies of ultra-flexible microemulsions", *J. Appl. Crystallogr.* **49** (2016), pp. 2063–2072.

[28] H. F. Eicke, H. Hammerich and G. Vasta, "A thermodynamic analysis of the molar conductivity of the ternary system: Water-aerosol OT-isooctane", *J. Colloid Interface Sci.* **93** (1983), pp. 593–595.

[29] J. Schmidt, R. Prignitz, D. Peschka, A. Münch, B. Wagner, E. Bänsch and W. Peukert, "Conductivity in nonpolar media: Experimental and numerical studies on sodium AOT–hexadecane, lecithin–hexadecane and aluminum(III)-3,5-diisopropyl salicylate–hexadecane systems", *J. Colloid Interface Sci.* **386** (2012), pp. 240–251.

[30] B. Lagourette, J. Peyrelasse, C. Boned and M. Clausse, "Percolative conduction in microemulsion type systems", *Nature* **281** (1979), pp. 60–62.

[31] M. Clausse, J. Peyrelasse, J. Heil, C. Boned and B. Lagourette, "Bicontinuous structure zones in microemulsions", *Nature* **293** (1981), pp. 636–638.

[32] A. Bumajdad and J. Eastoe, "Conductivity of mixed surfactant water-in-oil microemulsions", *Phys. Chem. Chem. Phys.* **6** (2004), pp. 1597–1602.

[33] H. F. Eicke, M. Borkovec and B. Das-Gupta, "Conductivity of water-in-oil microemulsions: a quantitative charge fluctuation model", *J. Phys. Chem.* **93** (1989), pp. 314–317.

[34] R. Fernández-Prini, "Solubility in fluids close to their critical points", *Pure Appl. Chem.* **67** (1995), pp. 519–526.

[35] K. I. Gutkowski, R. Fernández-Prini and M. L. Japas, "Solubility of solids in near-critical conditions: Effect of a third component", *J. Phys. Chem. B* **112** (2008), pp. 5671–5679.

[36] J. Frenkel, "A general theory of heterophase fluctuations and pretransition phenomena", *J. Chem. Phys.* **7** (1939), pp. 538–547.

[37] S. Kuke, B. Marmodée, S. Eidner, U. Schilde and M. U. Kumke, "Intramolecular deactivation processes in complexes of salicylic acid or glycolic acid with Eu(III)", *Spectrochim. Acta A: Mol. Biomol. Spectrosc.* **75** (2010), pp. 1333–1340.

[38] N. Aoyagi, T. Toraishi, G. Geipel, H. Hotokezaka, S. Nagasaki and S. Tanaka, "Fluorescence characteristics of complex formation of europium(III)-salicylate", *Radiochim. Acta* **92** (2004), pp. 589–593.

[39] H. M. N. H. Irving and S. P. Sinha, "The formation constants of europium(III)-salicylate complexes and their extraction into isoamyl alcohol", *Anal. Chim. Acta* **49** (1970), pp. 449–454.

[40] T. Toraishi, S. Nagasaki and S. Tanaka, "A theoretical study on molecular structure of Eu(III)-salicylate complexes in aqueous system", *J. Mol. Struct. Theochem.* **757** (2005), pp. 87–97.

[41] Z. L. Ernst and P. J. Newman, "Spectrophotometric determination of association constant of lanthanum salicylate", *Trans. Faraday Soc.* **64** (1968), pp. 1052–1058.

[42] Y. Hasegawa, N. Yamazaki, S. Usui and G. R. Choppin, "Effects of phenyl groups on thermodynamic parameters of lanthanoid(III) complexation with aromatic carboxylic acids", *Bull. Chem. Soc. Japan* **63** (1990), pp. 2169–2172.

[43] Y. Hasegawa, Y. Morita, M. Hase and M. Nagata, "Complexation of lanthanoid (III) with substituted benzoic or phenylacetic acids and extraction of these acids", *Bull. Chem. Soc. Japan* **62** (1989), pp. 1486–1491.

[44] S. W. X. H. L. Shengli, "Spectra of rare earth complexes with salicylate", *Acta Photonica Sinica* **35** (2006), pp. 1593–1596.

[45] P. Degot, V. Huber, A. El Maangar, et al., "Triple role of sodium salicylate in solubilization, extraction, and stabilization of curcumin from Curcuma longa", *J. Mol. Liq.* **329** (2021), article no. 115538.

[46] G. Förster, A. Meister and A. Blume, "Chain packing modes in crystalline surfactant and lipid bilayers", *Curr. Opin. Colloid Interface Sci.* **6** (2001), pp. 294–302.

[47] T. N. Zemb, M. Klossek, T. Lopian, et al., "How to explain microemulsions formed by solvent mixtures without conventional surfactants", *Proc. Natl. Acad. Sci. USA* **113** (2016), pp. 4260–4265.

[48] T. Lopian, S. Schöttl, S. Prévost, S. Pellet-Rostaing, D. Horinek, W. Kunz and T. Zemb, "Morphologies observed in ultraflexible microemulsions with and without the presence of a strong acid", *ACS Central Sci.* **2** (2016), pp. 467–475.

[49] M. L. Klossek, D. Touraud, T. Zemb and W. Kunz, "Structure and solubility in surfactant-free microemulsions", *ChemPhysChem.* **13** (2012), pp. 4116–4119.

[50] D. Subramanian and M. A. Anisimov, "Phase behavior and mesoscale solubilization in aqueous solutions of hydrotropes", *Fluid Phase Equilib.* **362** (2014), pp. 170–176.

[51] J. B. Hayter, "A self-consistent theory of dressed micelles", *Langmuir* **8** (1992), pp. 2873–2876.

[52] C. Erlinger, L. Belloni, T. Zemb and C. Madic, "Attractive interactions between reverse aggregates and phase separation in concentrated malonamide extractant solutions", *Langmuir* **15** (1999), pp. 2290–2300.

[53] M. Špadina, K. Bohinc, T. Zemb and J.-F. Dufrêche, "Multicomponent model for the prediction of nuclear waste/rare-earth extraction processes", *Langmuir* **34** (2018), pp. 10434–10447.

[54] B. J. Gullekson, A. T. Breshears, M. A. Brown, J. B. Essner, G. A. Baker, J. R. Walensky, A. Paulenova and A. V. Gelis, "Extraction of water and speciation of trivalent lanthanides and americium in organophosphorus extractants", *Inorg. Chem.* **55** (2016), pp. 12675–12685.

[55] B. Gannaz, M. R. Antonio, R. Chiarizia, C. Hill and G. Cote, "Structural study of trivalent lanthanide and actinide complexes formed upon solvent extraction", *Dalton Trans.* **38** (2006), pp. 4553–4562.

[56] W. Bu, H. Yu, G. Luo, et al., "Observation of a rare earth ion-extractant complex arrested at the oil–water interface during solvent extraction", *J. Phys. Chem. B* **118** (2014), pp. 10662–10674.

[57] D. Darvishi, D. F. Haghshenas, S. Etemadi, E. K. Alamdari and S. K. Sadrnezhaad, "Water adsorption in the organic phase for the D2EHPA–kerosene/water and aqueous Zn2+, Co2+, Ni2+ sulphate systems", *Hydrometallurgy* **88** (2007), pp. 92–97.

[58] H. Wennerström, "Micelles. Physical chemistry of surfactant association", *Phys. Rep.* **52** (1979), pp. 1–86.

[59] H. F. Eicke, M. Borkovec and B. Das-Gupta, "Conductivity of water-in-oil microemulsions: a quantitative charge fluctuation model", *J. Phys. Chem.* **93** (1989), pp. 314–317.

[60] T. Zemb, C. Bauer, P. Bauduin, et al., "Recycling metals by controlled transfer of ionic species between complex fluids: en route to "ienaics"", *Colloid. Polym. Sci.* **293** (2015), pp. 1–22.